applied optics

Terahertz spoof surface plasmonic demultiplexer based on band-stop waveguide units

Huilin Li, Yanfeng Li,* Mingrui Yuan, Xinyu Ma, and Jiaguang Han

Center for Terahertz Waves, Key Laboratory of Optoelectronics Information and Technology (Ministry of Education of China), College of Precision Instrument and Optoelectronics Engineering, Tianjin University, Tianjin 300072, China
**Corresponding author: yanfengli@tju.edu.cn*

Received 2 February 2022; revised 28 March 2022; accepted 20 April 2022; posted 21 April 2022; published 9 May 2022

Demultiplexers play an important role in wavelength division multiplexing optical transmission systems and constitute an essential component of future terahertz integrated circuits. In this work, we propose a terahertz spoof surface plasmonic demultiplexer, which is capable of distinguishing between three different frequencies by exploiting the band-stop effect of the waveguide units. The waveguide units are composed of metallic pillars of different sizes, where the transmission of spoof surface plasmons in the terahertz range is strongly influenced by the pillar size. The frequency-splitting feature can be achieved by selecting waveguide units with proper parameters that allow the passbands of the waveguides to be completely non-overlapping. As the effective working section, the length of the band-stop units is 1 mm, and extinction ratios of 21.5 dB, 18.0 dB, and 23.9 dB are obtained at 0.578 THz, 0.632 THz, and 0.683 THz, respectively. The proposed band-stop unit and its tunable characteristics have important applications for further development of terahertz integrated communication systems and terahertz on-chip plasmonic circuity.

https://doi.org/10.1364/AO.455430

1. INTRODUCTION

Terahertz (THz) waves are characterized by many unique properties, including high transmission through opaque materials, low photon energy, and the ability to discriminate between materials, which make them of great value in imaging, spectroscopy, biosensing, and security screening applications [1–6]. In addition, due to their broadband nature and the capability to carry massive information, THz waves are supposed to play an important role in next-generation ultra-high-speed communications [7–10]. However, the development of THz technology is still constrained by the lack of functional devices, the size of the devices is typically large accompanied by phase mismatch, and the free-space optical path occupies too much space [11,12]. Therefore, it is essential to develop miniaturized and compact functional components in the THz band.

Surface plasmon polaritons (SPPs) are a form of localized surface waves induced by the collective oscillations of electrons coupled with electromagnetic fields at a metal–dielectric interface [13]. Due to their remarkable local field enhancement and surface confinement properties, SPPs contribute to the significant reduction of optical device sizes and fine-tuning of THz waves at subwavelength scales, which is currently a frontier of research interest in the field of THz science and technology [14–17]. However, because metals behave almost as perfect electric conductors in the THz band, well-confined surface electromagnetic waves cannot be obtained in this important frequency range [18,19].

It has been shown that by fabricating periodic grooves or structures on the surface of ideal conductors, bound-state electromagnetic waves with properties similar to those of SPPs in the visible band can be obtained in these structured metallic surfaces in the THz band. Such well-bound electromagnetic surface waves are defined as spoof surface plasmon polaritons (SSPPs) [20–25] and are currently implemented mostly by domino structures, one-dimensional groove arrays, two-dimensional hole arrays, V-shaped grooves, and many others [26–29]. Spoof plasmonic devices based on these structures can contribute to potential miniaturized and compact functional components in the THz band.

Wavelength division multiplexing (WDM) technology is crucial in optical transmission systems because of its ability to satisfy the rapidly growing demand for high-capacity data transmission, and is also essential for future THz integrated circuits [30,31]. Currently, it is common to adopt diffraction grating coupling or micro-ring resonator filtering to achieve frequency differentiation, while directional couplers have also been used for wavelength duplexer functions [32–34]. However, among the above solutions, the diffraction grating coupling and directional coupling approaches in the THz band can currently only distinguish between and generate two-wavelength outputs simultaneously, while micro-ring resonators are limited by the free spectral range and have a large bending loss [35]. To reduce the device size and improve compactness, particle swarm optimization and inverse design algorithms are also used in the

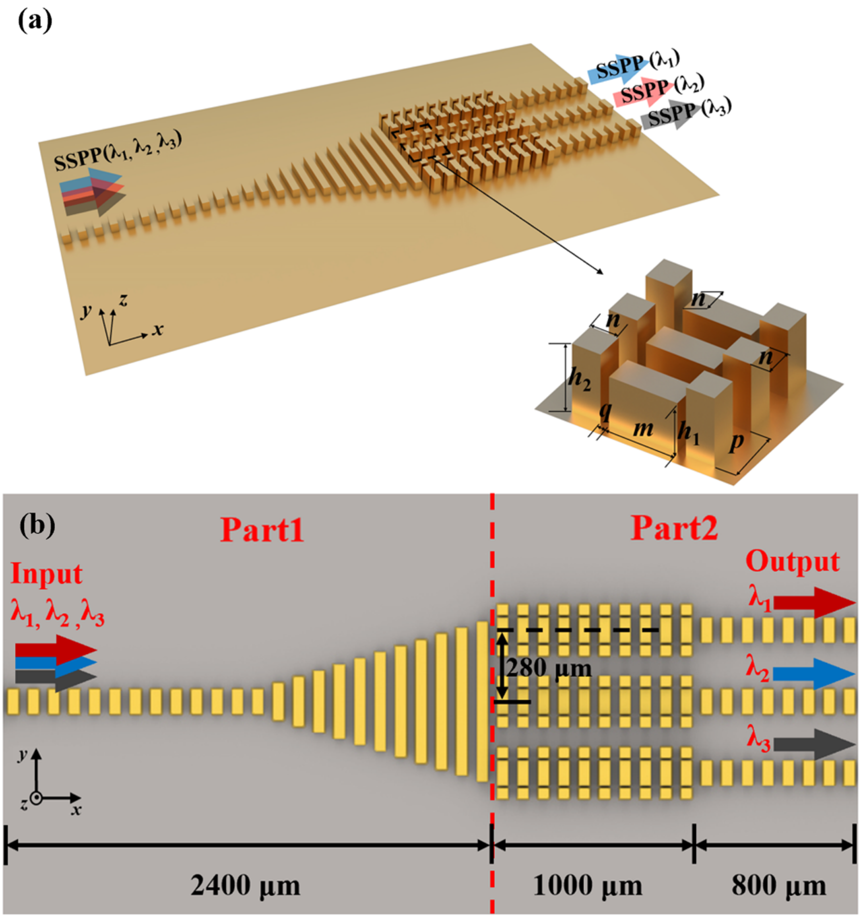

Fig. 1. Demultiplexer design and waveguide unit. (a) Three-dimensional view of the device and zoomed-in waveguide unit and (b) two-dimensional detailed view of the whole structure. Different colored arrows delineate the propagation paths of SSPPs at three different wavelengths (frequencies).

design of demultiplexers [36–39]. However, the design process of these algorithms is quite complex and limited in bandwidth.

In this work, we report a three-port THz demultiplexer based on SSPP waveguide units with a band-stop function. The basic idea is to exploit the fact that the SSPP transmission in a rectangular metallic pillar waveguide is determined by the waveguide dimensions. The function of separating three different frequencies is achieved by combining band-stop waveguide units with proper parameters that allow the passbands of these waveguides to be completely non-overlapping. Our design strategy is expected to be of great use for other key THz plasmonic devices.

2. STRUCTURE DESIGN AND DEVICE CHARACTERIZATION

As schematically illustrated in Fig. 1, our demultiplexer is based on waveguide structures composed of rectangular metallic pillars of different sizes, which are used to implement the function of frequency selection. The whole device consists of two parts, the transmission section (Part 1) and the frequency selection section (Part 2), as shown in Fig. 1(b). In the transmission section, the excited SSPPs propagate to the input port of the frequency selection section using a rectangular metallic pillar waveguide with a gradually increasing width. It is worth noting that the size and shape of the transmission section can be flexibly adjusted in practical applications. The frequency selection section consists of three rows of concave-shaped waveguide units [inset in Fig. 1(a)] with a rectangular metallic pillar waveguide attached behind each of them, and all the structures are arranged in a domino configuration. The concave-shaped waveguide units play the role of frequency selection, and the rectangular metallic pillars serve as the output waveguides.

The concave-shaped structure unit of our design is schematically depicted in the inset of Fig. 1(a) with all the structural parameters defined. It consists of two higher square metallic pillars on both sides and a lower rectangular pillar in the middle, where the higher pillar height is $h_2 = 120$ μm, the lower pillar length is $m = 120$ μm, and the width of both pillars is $n = 50$ μm. The interval between two pillars is $q = 15$ μm in the y direction for each concave-shaped unit, and the period is $p = 100$ μm in the transmission direction (i.e., the x direction). The heights of the middle lower pillars h_1 from top to bottom are finally chosen to be 90, 70, and 110 μm, respectively; the order is selected to avoid crosstalk between two adjacent frequencies. The basis for the selection of the above specific parameters will be given in the subsequent discussion. The total length is 2.4 mm for the transmission section and 1.8 mm

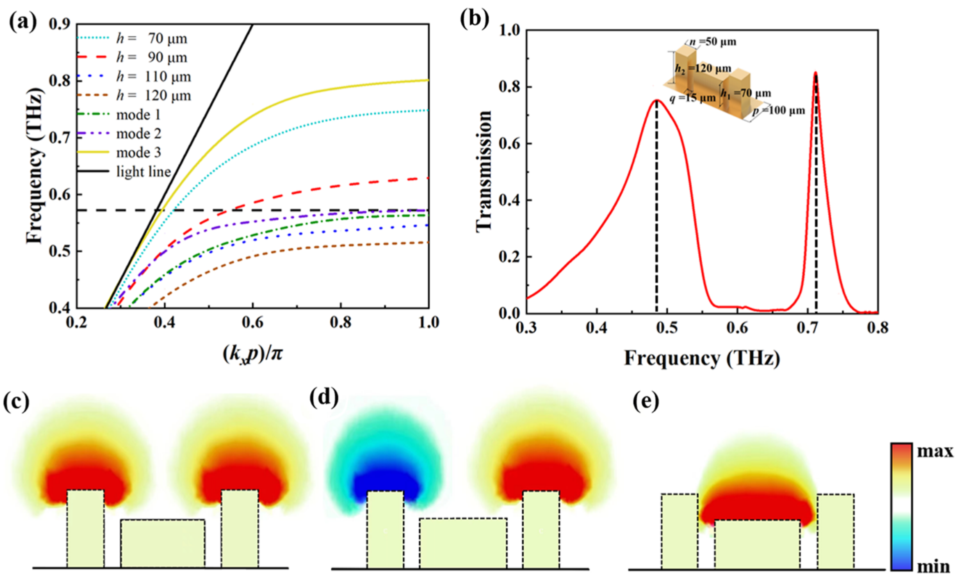

Fig. 2. Dispersion analysis of the waveguide unit and transmission property of the band-stop waveguide. (a) Dispersion curves for metallic pillars of different heights and for different modes supported by the concave-shaped waveguide unit, where the horizontal dashed line is the cutoff frequency for the concave-shaped unit. (b) Transmission of a band-stop waveguide composed of concave-shaped units with parameters as defined in the inset. The electric field is calculated at 100 µm (which is much smaller than the penetration depth of the exponentially decaying field) above the waveguide by the time-domain solver of CST Microwave Studio. (c)–(e) Normalized electric field distributions in the yz cross section for the symmetric mode (c) [mode 1 in (a)] and anti-symmetric mode (d) [mode 2 in (a)] at 0.48 THz and the fundamental mode (e) [mode 3 in (a)] at 0.71 THz. These two frequencies are respectively chosen to be at the centers of the low- and high-frequency transmission bands, shown by the dashed lines in (b).

for the frequency selection section. As the effective working section, the length of the concave-shaped waveguide units is only 1 mm, which is 7.6% of a conventional wavelength duplexer [40]. When broadband SSPPs enter the input port, the three output ports export SSPPs at 0.632 THz, 0.683 THz, and 0.578 THz from top to bottom, respectively. The detailed working principles are discussed below.

The basic unit of the SSPP waveguides is a subwavelength metallic rectangular pillar on a metal plate [41–44]. The domino structure is adopted for the following reasons: (1) Compared with coplanar strip designs [29,45,46], the electric field of the 3D structure is mainly in the z direction, thus enabling direct measurement and characterization of the SSPP propagation process using a near-field scanning THz microscope, as described elsewhere [47]. (2) This structure supports the propagation of well-confined SSPPs, and its dispersion can be adjusted by changing the unit parameters such as its height, width, and period, facilitating the realization of complex and diverse functions. (3) Additional functions such as SSPP excitation and focusing can be integrated onto the same platform by standard lithography, etching, and metal sputtering fabrication techniques, as shown in [34,40].

The dispersion curves of a rectangular metallic waveguide unit cell with period $p = 100$ µm, length $m = 120$ µm, and width $n = 50$ µm for different pillar heights are studied by the eigenmode solver of the commercial software CST Microwave Studio. Periodic boundary conditions are used in the simulation of a unit cell, and metal is treated as a perfect electric conductor, which is a valid assumption in the THz frequency range, as a typical metal exhibits very low loss and allows a propagation length of hundreds of meters [48]. The phase θ in the propagation direction is calculated from 0° to 180° with a step of 10°, and the value of the propagation constant k_x can be calculated according to $k_x = \theta \times \pi/(180 \times p)$.

Investigation of the simulation results for an individual metallic pillar in Fig. 2(a) shows that the SSPP dispersion curve is strongly affected by the pillar height, as can be seen in the dashed curves in Fig. 2(a). In particular, the higher the pillar height, the greater the curve deviates from the light line, and meanwhile the lower the cutoff frequency. Higher-frequency signals above the cutoff frequency cannot propagate through the waveguide pillars. Therefore, by placing pillars with a suitable height difference within a waveguide unit [as shown in the inset of Fig. 1(a)], it is possible to induce a band-stop effect by creating a blocked frequency range between the cutoff frequency of the higher pillar and the strongly bound frequency of the lower pillar.

The transmission of a waveguide composed of such concave-shaped units is simulated and presented in Fig. 2(b), where the detailed parameters are given in the inset. A band-stop function is clearly observed and can be understood as follows. The dispersion curves for such a composite unit are plotted in Fig. 2(a) as the colored solid line and dashed–dotted lines. In the low-frequency transmission range with a cutoff frequency range around 0.57 THz, this concave-shaped structure unit is capable of supporting the propagation of two modes, modes 1 and 2. These two modes can be understood as the symmetric and anti-symmetric modes that propagate along the two higher pillars, respectively. These two higher pillars are separated by the lower pillar and are weakly coupled, and this explanation in terms of super-modes is well understood in coupled mode

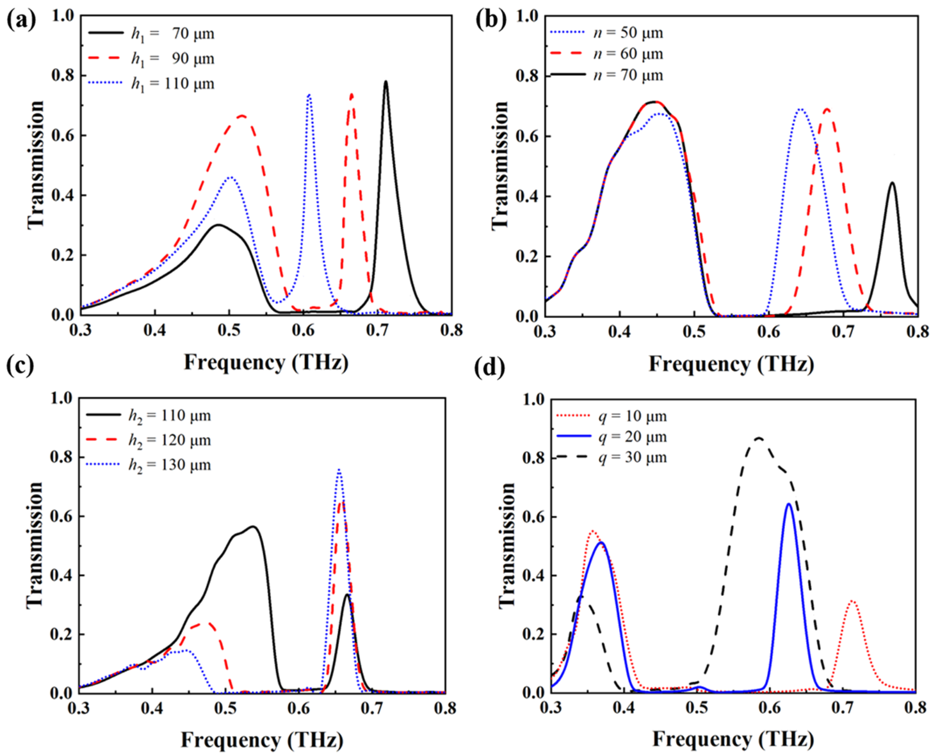

Fig. 3. Variation of the transmission of a band-stop waveguide composed of concave-shaped units when the (a) lower pillar height, (b) width of both pillars, (c) higher pillar height, or (d) interval between pillars in the waveguide unit is varied. The default parameters in the simulation are $p = 100$ μm, $m = 120$ μm, $h_1 = 80$ μm, $n = 50$ μm, $h_2 = 120$ μm, and $q = 20$ μm.

theory. The mode field distributions are exemplified in Figs. 2(c) and 2(d), respectively, at the center frequency of 0.48 THz of the low-frequency transmission band of Fig. 2(b). The two modes gradually approach a single cutoff frequency. This is understandable as these two modes will no longer be coupled and resemble the mode supported by a single higher pillar. However, the cutoff frequency of this composite structure is larger that of a single metallic pillar with $h = 120$ μm due to the presence of the central lower pillar. At the same time, one can observe from Fig. 2(a) that another mode (mode 3) is also supported by the composite structure. From the field distribution shown in Fig. 2(e) at the center frequency of 0.71 THz of the high-frequency transmission band of Fig. 2(b), this mode is the fundamental mode supported by the central lower pillar in the unit. This is also supported by the fact that its dispersion curve is close to that of a singular pillar with $h = 70$ μm, as can be seen in Fig. 2(a). When the frequency of the SSPPs exceeds the cutoff frequency of the higher pillars, they cannot propagate through the unit even through the lower pillar, because the dispersion curve of mode 3 is so close to the light line that the localization of the SSPPs by the structure is too weak. With a further increase of frequency, the central pillar starts to support a well-localized field and the SSPPs can propagate mainly through the lower pillar alone. In particular, the two higher pillars form a kind of cavity, which helps to confine the SSPP field in the middle. This explains why the higher-frequency transmission is sharper. In short, the band-stop effect is attributed to the combined transmissions through the bilateral pillars and the central pillar.

To understand the transmission (i.e., band-stop) properties of the waveguide based on the concave-shaped units and its application in THz WDM technology, we have further investigated the influence on the stop band by the variation of the multiple parameters of the concave-shaped structure. Since the concave-shaped structure is composed of three independent metallic pillars of two kinds, the sizes of each kind of pillar and the interval between the pillars can be varied independently. The effects of the variations of the parameters on the stop band are shown in Fig. 3, where the default parameters are $p = 100$ μm, $m = 120$ μm, $h_1 = 80$ μm, $n = 50$ μm, $h_2 = 120$ μm, and $q = 20$ μm. It is found that among all these parameters, the change in height of the lower pillar h_1 has the most significant effect on the stop band [Fig. 3(a)]. If the other parameters are fixed, the width of the stop band is narrowed as the height of the lower pillar is increased because the lower-frequency passband is roughly unchanged whereas the higher-frequency passband has a continual red shift. The change of the pillar width n mainly shifts the high-frequency passband [see Fig. 3(b)]. On the other hand, the height variation of the higher pillar h_2 mainly has a modulating effect on the width of the stop band, as can be seen in Fig. 3(c). In addition, the change of the interval q between the pillars can simultaneously affect the amplitude, bandwidth, and center frequency of the high-frequency passband [Fig. 3(d)]. The impact of these parameters on the stop band can be understood from the previous discussion related to the results of Fig. 2. In view of the results of Fig. 3, the parameters of the waveguide units can be chosen such that the target transmission frequencies fall within the highly tunable higher-frequency passband

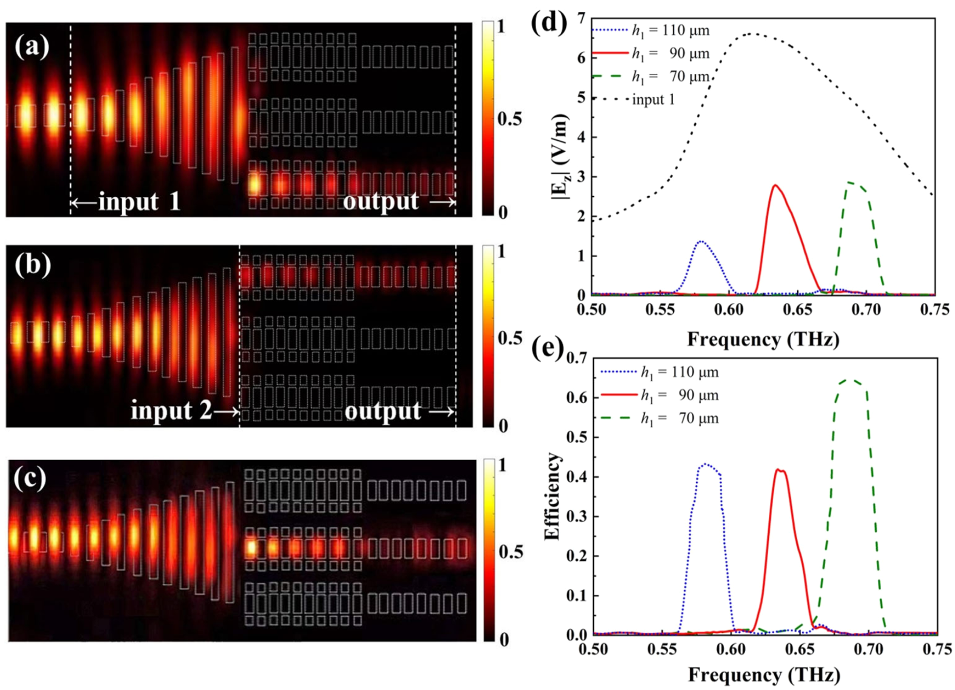

Fig. 4. (a)–(c) Simulations obtained for the normalized $|E_z|^2$ distributions corresponding to (a) $f = 0.578$ THz, (b) $f = 0.632$ THz, and (c) $f = 0.683$ THz in a horizontal plane at 170 μm above the substrate surface of the structure. (d) Normalized electric field and (e) efficiency of the demultiplexer at the output port.

to achieve a narrowband and efficient WDM function. The center frequency range is set around 0.6 THz and the lower pillar heights in the waveguides from top to bottom in Fig. 1 are specifically chosen to be 90, 70, and 110 μm, respectively. As can be seen from Fig. 3(a), the high-frequency ranges over which the SSPPs are allowed to pass through the three waveguides do not overlap, and thus such a device can act as a highly efficient frequency selector.

For application and verification of the principles described above, we connect three rows of such waveguides with different dimensions to the excitation and output ports of the SSPPs, as illustrated in Fig. 1(b). All the parameters in the three pillars of these waveguides are the same except the height of the lower pillars. To verify the functionality of the demultiplexer, simulations are performed with the time domain solver. The simulated results for the normalized $|E_z|^2$ distributions of the demultiplexer with a scan area of 5 mm × 2 mm are shown in Figs. 4(a)–4(c) at $f = 0.578$ THz, $f = 0.632$ THz, and (c) $f = 0.683$ THz, respectively. As can be seen in these distributions, the demultiplexer function is effectively achieved by the frequency selection section (Part 2 in Fig. 1), i.e., the waveguides composed of concave-shaped units. The normalized electric fields are shown in Fig. 4(d), where three narrow non-overlapping passbands are clearly separated. The input and output spectra are calculated respectively along the dashed lines in Fig. 4(a), and the probes are placed at 100 μm above the device.

The performance of this demultiplexer is evaluated by the extinction ratio (ER), insertion loss (IL), and transmission efficiency within each operation frequency range. The extinction ratio is calculated as $\mathrm{ER} = 10\log(P_1/P_2)$, where P_1 indicates the power at an output port for the corresponding transmission frequency and P_2 represents the larger energy at this particular frequency at the other two output waveguides. Values of ER of 21.5 dB, 18.0 dB, and 23.9 dB can be acquired at 0.578 THz, 0.632 THz, and 0.683 THz, respectively. And within a 30 GHz bandwidth range, the extinction ratios are higher than 15.5 dB, 15.3 dB, and 16.1 dB, respectively. The IL of each channel in Part 2 is derived by comparing the loss of the structure with that of a straight waveguide of the same length, and the loss is calculated as $10\log(P_{\mathrm{in}}/P_{\mathrm{out}})$, where P_{in} and P_{out} are the input and output powers calculated along the white lines indicated in Fig. 4(b), respectively. The IL values are 0.88 dB, 0.87 dB, and 0.75 dB at 0.578 THz, 0.632 THz, and 0.683 THz, respectively. In addition to the IL of each channel, the total loss of the device also includes the transmission loss of Part 1 and the beam-splitting loss at the connection between Part 1 and Part 2. Since the equivalent refractive index of the SSPP mode is insensitive to the lateral width change of the waveguide pillar, the SSPPs are able to transmit efficiently in the straight waveguide and the funnel-shaped waveguide with a lateral mode size transition. The losses in the straight and funnel waveguide sections are calculated to be 1.34 dB/mm and 1.47 dB/mm, respectively. The beam-splitting loss is estimated to be around 4.7 dB, due to the very simple design with the wide waveguide in Part 1 connected to the three channels in Part 2, and can in principle be eliminated or reduced with an improved approach. The efficiency for the three waveguides is shown in Fig. 4(e), which is calculated as $P_{\mathrm{out}}/P_{\mathrm{in}}$ for each waveguide. The calculation of power is performed by integrating the longitudinal components of the Poynting vector in the vertical planes [indicated as the dashed lines in Fig. 4(b)] placed near the input and the output of the demultiplexer. The integration regions have an identical size of 400 μm × 400 μm, which is chosen to be larger than the maximum size of the mode so as to guarantee accurate calculation of the power distribution. The performance of the device for WDM demultiplexing is well validated by the results presented in Fig. 4.

Previously, domino structures were fabricated on silicon wafers using photolithography and deep reactive ion etching, followed by metal sputtering [34,40]. Since the demultiplexer in this design requires different waveguide heights, its fabrication is very challenging but can be envisaged by using other techniques such as 3D printing techniques or direct laser writing.

3. CONCLUSION

In summary, we propose and design a compact and high-extinction-ratio demultiplexer that enables effective control of SSPPs in the THz band. The device is mainly composed of plasmonic waveguides based on a combination of three metallic pillars, which form a concave structure and induce a band-stop effect. Multiple frequencies can be filtered out by selecting waveguide units with proper sizes. The effective working length of the device is only 1 mm, and the extinction ratio is up to 23.9 dB. In addition, the proposed structure can be integrated into THz plasmonic on-chip systems, and these components are expected to be of significant value for future THz communication applications.

Funding. National Key Research and Development Program of China (2017YFA0701004); National Natural Science Foundation of China (61735012, 61875150, 61935015, 62025504); Tianjin Municipal Fund for Distinguished Young Scholars (18JCJQJC45600).

Disclosures. The authors declare no conflicts of interest.

Data availability. All data included in this study are available upon request by contact with the corresponding author.

REFERENCES

1. T. Kampfrath, K. Tanaka, and K. A. Nelson, “Resonant and nonresonant control over matter and light by intense terahertz transients,” Nat. Photonics **7**, 680–690 (2013).
2. M. C. Hoffmann and J. A. Fülöp, “Intense ultrashort terahertz pulses: generation and applications,” J. Phys. D **44**, 083001 (2011).
3. X. Yang, X. Zhao, K. Yang, Y. P. Liu, Y. Liu, W. Fu, and Y. Luo, “Biomedical applications of terahertz spectroscopy and imaging,” Trends Biotechnol. **34**, 810–824 (2016).
4. L. Minkevičius, D. Jokubauskis, I. Kašalynas, S. Orlov, A. Urbas, and G. Valušis, “Bessel terahertz imaging with enhanced contrast realized by silicon multi-phase diffractive optics,” Opt. Express **27**, 36358–36367 (2019).
5. S. Preu, G. H. Döhler, S. Malzer, L. J. Wang, and A. C. Gossard, “Tunable, continuous-wave terahertz photomixer sources and applications,” J. Appl. Phys. **109**, 061301 (2011).
6. H. Guerboukha, K. Nallappan, and M. Skorobogatiy, “Toward real-time terahertz imaging,” Adv. Opt. Photon. **10**, 843–938 (2018).
7. T. Kleine-Ostmann and T. Nagatsuma, “A review on terahertz communications research,” J. Infrared Millim. Terahertz Waves **32**, 143–171 (2011).
8. T. Nagatsuma, G. Ducournau, and C. C. Renaud, “Advances in terahertz communications accelerated by photonics,” Nat. Photonics **10**, 371–379 (2016).
9. S. Ummethala, T. Harter, K. Koehnle, Z. Li, S. Muehlbrandt, Y. Kutuvantavida, J. Kemal, P. Marin-Palomo, J. Schaefer, A. Tessmann, S. K. Garlapati, A. Bacher, L. Hahn, M. Walther, T. Zwick, S. Randel, W. Freude, and C. Koos, “THz-to-optical conversion in wireless communications using an ultra-broadband plasmonic modulator,” Nat. Photonics **13**, 519–524 (2019).
10. T. Nagatsuma, S. Horiguchi, Y. Minamikata, Y. Yoshimizu, S. Hisatake, S. Kuwano, N. Yoshimoto, J. Terada, and H. Takahashi, “Terahertz wireless communications based on photonics technologies,” Opt. Express **21**, 23736–23747 (2013).
11. X. Lu and X. C. Zhang, “Investigation of ultra-broadband terahertz time-domain spectroscopy with terahertz wave gas photonics,” Front. Optoelectron. **7**, 121–155 (2014).
12. K. Sato and Y. Monnai, “Terahertz beam steering based on trajectory deflection in dielectric-free Luneburg lens,” IEEE Trans. Terahertz Sci. Technol. **10**, 229–236 (2020).
13. W. L. Barnes, A. Dereux, and T. W. Ebbesen, “Surface plasmon subwavelength optics,” Nature **424**, 824–830 (2003).
14. S. Kasani, K. Curtin, and N. Wu, “A review of 2D and 3D plasmonic nanostructure array patterns: fabrication, light management and sensing applications,” Nanophotonics **8**, 2065–2089 (2019).
15. E. Ozbay, “Plasmonics: merging photonics and electronics at nanoscale dimensions,” Science **311**, 189–193 (2006).
16. J. Zhang, L. Zhang, and W. Xu, “Surface plasmon polaritons: physics and applications,” J. Phys. D **45**, 113001 (2012).
17. T. Yang, Y. Zhou, X. A. Li, W. Huang, Y. Qin, Y. Zhu, and H. Ho, “Optical modulation of terahertz surface plasmon propagated on surfaces of semiconductors,” in *IEEE International Conference on Electron Devices and Solid-State Circuits (EDSSC)* (2015), pp. 337–340.
18. J. Saxler, J. G. Rivas, C. Janke, H. P. M. Pellemans, P. H. Bolívar, and H. Kurz, “Time-domain measurements of surface plasmon polaritons in the terahertz frequency range,” Phys. Rev. B **69**, 155427 (2004).
19. T. I. Jeon and D. Grischkowsky, “THz Zenneck surface wave (THz surface plasmon) propagation on a metal sheet,” Appl. Phys. Lett. **88**, 061113 (2006).
20. J. B. Pendry, L. Martin-Moreno, and F. J. Garcia-Vidal, “Mimicking surface plasmons with structured surfaces,” Science **305**, 847–848 (2004).
21. J. J. Wood, L. A. Tomlinson, O. Hess, S. A. Maier, and A. I. Fernández-Domínguez, “Spoof plasmon polaritons in slanted geometries,” Phys. Rev. B **85**, 075441 (2012).
22. S. A. Maier, S. R. Andrews, L. Martin-Moreno, and F. J. Garcia-Vidal, “Terahertz surface plasmon polariton propagation and focusing on periodically corrugated metal wires,” Phys. Rev. Lett. **97**, 176805 (2006).
23. L. Shen, X. Chen, and T. J. Yang, “Terahertz surface plasmon polaritons on periodically corrugated metal surfaces,” Opt. Express **16**, 3326–3333 (2008).
24. L. Liu, Z. Li, B. Xu, C. Gu, C. Chen, P. Ning, J. Yan, and X. Chen, “High-efficiency transition between rectangular waveguide and domino plasmonic waveguide,” AIP Adv. **5**, 027105 (2015).
25. B. You, C. C. Peng, J. Jhang, H. H. Chen, C. P. Yu, W. C. Lai, T. A. Liu, J. L. Peng, and J. Y. Lu, “Terahertz plasmonic waveguide based on metal rod arrays for nanofilm sensing,” Opt. Express **22**, 11340–11350 (2014).
26. Z. Ruan and Q. Min, “Slow electromagnetic wave guided in subwavelength region along one-dimensional periodically structured metal surface,” Appl. Phys. Lett. **90**, 201906 (2007).
27. Z. Gao, L. Shen, J. J. Wu, T. J. Yang, and X. Zheng, “Terahertz surface plasmon polaritons in textured metal surfaces formed by square arrays of metallic pillars,” Opt. Commun. **285**, 2076–2080 (2012).
28. A. I. Fernández-Domínguez, E. Moreno, L. Martín-Moreno, and F. J. García-Vidal, “Guiding terahertz waves along subwavelength channels,” Phys. Rev. B **79**, 233104 (2009).
29. H. Ma, X. Shen, Q. Cheng, W. Jiang, and T. Cui, “Broadband and high-efficiency conversion from guided waves to spoof surface plasmon polaritons,” Laser Photon. Rev. **8**, 146–151 (2014).
30. G. E. Keiser, “A review of WDM technology and applications,” Opt. Fiber Technol. **5**, 3–39 (1999).
31. P. J. Winzer and R. J. Essiambre, “Advanced modulation formats for high-capacity optical transport networks,” J. Lightwave. Technol. **24**, 4711–4728 (2006).
32. S. F. Busch, S. Schumann, C. Jansen, M. Scheller, M. Koch, and B. M. Fischer, “Optically gated tunable terahertz filters,” Appl. Phys. Lett. **100**, 261109 (2012).

33. R. K. Jaiswal, N. Pandit, and N. P. Pathak, "Terahertz plasmonic metamaterial based multi-band band-pass filter using micro-ring resonator," in *USNC-URSI Radio Science Meeting (Joint with AP-S Symposium)* (2019), pp. 3–4.
34. M. Yuan, Q. Wang, Y. Li, X. Zhang, J. Han, and W. Zhang, "Ultra-compact terahertz plasmonic wavelength diplexer," Appl. Opt. **59**, 10451–10456 (2020).
35. Y. Xu and S. Pasricha, "Silicon nanophotonics for future multicore architectures: opportunities and challenges," IEEE Des. Test. **31**, 9–17 (2014).
36. M. Mohamadrezaee, M. Shirali, M. Akhlaghi, and M. Kaboli, "Combination of binary particle swarm optimization algorithm and discrete dipole approximation method to investigate the plasmonic circuit-based coherent perfect absorption filter," Opt. Quantum Electron. **49**, 100 (2017).
37. A. Y. Piggott, J. Lu, K. G. Lagoudakis, J. Petykiewicz, T. M. Babinec, and J. Vučković, "Inverse design and demonstration of a compact and broadband on-chip wavelength demultiplexer," Nat. Photonics **9**, 374–377 (2015).
38. S. H. Li and J. S. Li, "Compact multi-channel terahertz wave demultiplexer," in *12th International Symposium on Antennas, Propagation and Electromagnetic Theory (ISAPE)* (2018), pp.1–4.
39. G. Zhu, F. Huang, Z. Dai, X. Ju, S. Zhong, and X. Wang, "Reverse design of on-chip terahertz demultiplexers," Micromachines **12**, 1093 (2021).
40. Y. Zhang, Y. Xu, C. Tian, Q. Xu, X. Zhang, Y. Li, X. Zhang, J. Han, and W. Zhang, "Terahertz spoof surface-plasmon-polariton subwavelength waveguide," Photon. Res. **6**, 18–23 (2018).
41. G. Kumar, S. Li, M. M. Jadidi, and T. E. Murphy, "Terahertz surface plasmon waveguide based on a one-dimensional array of silicon pillars," New J. Phys. **15**, 085031 (2013).
42. D. Martin-Cano, M. L. Nesterov, A. I. Fernandez-Dominguez, F. J. Garcia-Vidal, L. Martin-Moreno, and E. Moreno, "Domino plasmons for subwavelength terahertz circuitry," Opt. Express **18**, 754–764 (2010).
43. W. Zhao, O. M. Eldaiki, R. Yang, and Z. Lu, "Deep subwavelength waveguiding and focusing based on designer surface plasmons," Opt. Express **18**, 21498–21503 (2010).
44. Y. G. Ma, L. Lan, S. M. Zhong, and C. K. Ong, "Experimental demonstration of subwavelength domino plasmon devices for compact high-frequency circuit," Opt. Express **19**, 21189–21198 (2011).
45. Y. Guo, X. Da, and K. Hou, "A two-way THz frequency splitter using CPS-based SSPPs," in *Cross Strait Quad-Regional Radio Science and Wireless Technology Conference (CSQRWC)* (2018).
46. Y. Guo, K. Xu, X. Deng, X. Cheng, and Q. Chen, "Millimeter-wave on-chip bandpass filter based on spoof surface plasmon polaritons," IEEE Electr. Device Lett. **41**, 1165–1168 (2020).
47. Y. Xu, X. Zhang, Z. Tian, J. Gu, C. Ouyang, Y. Li, J. Han, and W. Zhang, "Mapping the near-field propagation of surface plasmons on terahertz metasurfaces," Appl. Phys. Lett. **107**, 021105 (2015).
48. M. Gong, T. I. Jeon, and D. Grischkowsky, "THz surface wave collapse on coated metal surfaces," Opt. Express **17**, 17088–17101 (2009).